ADVANCED ENERGY MATERIALS
www.advenergymat.de

# Elemental Stability Rules for High Entropy Disordered Rocksalt Type Li-Ion Battery Positive Electrodes

*Lin Wang, Neelam Sunariwal, Yufang He, Do-hoon Kim, Dong-hee Yeon, Yan Zeng, Jordi Cabana, and Bin Ouyang**

**High entropy disordered rocksalt (HE-DRX) Li-ion battery positive electrodes have gained attention as a potential alternative to commercialized positive electrodes, aiming to eliminate or minimize the use of Ni/Co while maintaining competitive electrochemical performance. Despite their potential, understanding the intricate elemental stability across the vast HE-DRX chemical landscape remains a significant challenge. In this study, we tackle this challenge by conducting a comprehensive data-driven phase diagram analysis of 18810 potential HE-DRX compositions, each featuring common Li and F stoichiometries. Leveraging a charge balance algorithm, we systematically explore redox stability and phase stability, unveiling critical insights into chemical stability rules within the HE-DRX design space. The analysis also uncovers untapped potential of Cu as redox-active centers, with Sb and Sn contributing as stable charge compensators. The utilization of these elements is seldom reported in the literature but has been validated by the successful experimental synthesis of materials $Li_{21}Zr_3Ti_3Mn_2Fe_5Cu_2O_{36}$ and $Li_{21}Mn_2Ti_3Fe_5Cu_2Sn_3O_{36}$.**

## 1. Introduction

With the growing demand for portable devices and electric vehicles that rely on batteries as a power source, exploring more sustainable battery materials with good performance remains a primary goal. Particularly, the recent focus on Li-ion positive electrodes is centered on discovering materials with not only good performance, but also lower cost.[1–5] Introducing high entropy composition has emerged as a promising materials design strategy[6–8] to enable competitive performance as well as reduce or eliminate the utilization of critical elements, e.g., Co and Ni. This unique compositional space offers an effective strategy to minimize detrimental short-range order[7,9–11] and to introduce the lattice distortion in disordered rocksalt (DRX) type positive electrodes,[12] thereby improving Li percolation, enhancing Li kinetics, and reducing the volume change during cycling.[6,12,13] These improvements arise not from the presence of specific elements but from the collective contribution of a diverse ensemble of elements. To fully reach these advantages, it is essential to identify elements that exhibit stability and compatibility across a wide range of compositions.

Despite the promise of high-entropy disordered rocksalt (HE-DRX) positive electrodes, their development is hindered by the challenge of understanding the synthetic accessibility within the immense compositional space. In this study, we investigate the stability of HE-DRX positive electrode materials and aim to identify key stabilization rules. We picked six typical chemical formulas of HE-DRX that are studied[9,10,14] and enumerated all compositional possibilities within 28 cations derived from 13 metals, resulting in 18810 possible compounds. The exact equilibrium charge states of each species were discovered by density function theory and determined by our charge balance algorithm, which enabled us to chart both redox stability and phase stability of various ion species. Through comprehensive analysis of ion stability from different perspectives, it has been discovered that $Cu^{2+}$ is an overlooked redox center, which shows great stability among a diverse range of compositions. Meanwhile, $Sb^{5+}$ and $Sn^{4+}$ are found to be the overlooked charge compensators. Surprisingly and excitingly, both $Cu^{2+}$ as a redox center and $Sb^{5+}/Sn^{4+}$ as charge compensators are seldom reported in literature. To validate our computational stability investigation, we synthesized two HE-DRX compositions with these elements from our dataset: $Li_{21}Zr_3Ti_3Mn_2Fe_5Cu_2O_{36}$ and $Li_{21}Mn_2Ti_3Fe_5Cu_2Sn_3O_{36}$. The successful synthesis of these compounds reinforces the reliability of our computational approach and the stability of these overlooked elements.

## 2. Methodology

### 2.1. DFT Calculations

First-principles DFT calculations were performed to obtain an accurate description of the structural energies and magnetic

L. Wang, Y. He, Y. Zeng, B. Ouyang
Department of Chemistry and Biochemistry
Florida State University
Tallahassee, FL 32304, USA
E-mail: bouyang@fsu.edu
N. Sunariwal, J. Cabana
Department of Chemistry
University of Illinois at Chicago
Chicago, IL 60637, USA
D.-hoon Kim, D.-hee Yeon
Samsung SDI
Yeongtong-gu, Suwon-si, Gyeonggi-do 16678, South Korea
The ORCID identification number(s) for the author(s) of this article can be found under https://doi.org/10.1002/aenm.202404982

DOI: 10.1002/aenm.202404982

 

moments of the different positive electrode materials. All the calculations were performed using the projector-augmented wave (PAW) method[15] as implemented in the Vienna Ab initio Simulation Package (VASP).[16] The PAW potentials were based on the Perdew-Burke-Ernzerhof (PBE) form of the generalized gradient approximation (GGA) as the exchange-correlation functional. A rotationally averaged Hubbard U correction[17,18] was used to correct the self-interaction error in oxides containing Cr, Fe, Mn, Mo, and V. The U parameters were obtained from a previously reported calibration to oxide formation energies.[18] For all calculations, spin-polarized method was used, a reciprocal space discretization of 25 k-points per $Å^{-1}$ was applied, with a plane-wave cutoff energy of 520 eV, and the convergence criteria were set as $10^{-6}$ eV for electronic loops and 0.02 $eVÅ^{-1}$ for ionic loops.

### 2.2. Thermodynamic Stability

To investigate the thermodynamic stability of our calculated HE-DRX database. In each composition, all the entries with relative chemical space are extracted from the Materials Project[19] to build a convex hull of complete chemical space. The stability of phases not located on the hull is quantified by their energy above the hull ($E_{hull}$), which signifies the compound's tendency or driving force toward decomposition into their nearby ground states. $E_{hull}$ serves as a reasonable indicator of synthetic accessibility, as experimentally accessible materials must generally have a low $E_{hull}$ value.[20–22] To consider the influence of high entropy on thermodynamic stability, configuration entropy and temperature are involved in calculating the $E_{hull}$ at a specific temperature, $E_{hull,\,T} = E_{hull,\,0K} - TS_{Ideal}$. In this study, 1473K is used to estimate the typical upper bound temperature of solid-state synthesis in a typical muffle or tube furnace. When constructing the convex hull, an anion correction will be added to all entries.[18] At the same time, in our studied HE-DRX materials, metal oxides and metal fluorides always work as decomposition ground states, while $O_2$ and $F_2$ gases seldom show up. This feature further minimizes the potential issue of inaccurate calculation of $O_2$ and $F_2$ by GGA level of theory. The stabilization temperature is calculated and used as an indicator of synthetic accessibility; the distribution of the calculated stabilization temperature is shown in Figure S1 (Supporting Information).

### 2.3. Material Synthesis

All the HE-DRX oxides were synthesized by the traditional solid-state method. $Li_2CO_3$ (Sigma–Aldrich, 99.999%), $TiO_2$ (Sigma–Aldrich, 99.8%), $MnO_2$ (Sigma–Aldrich, 99%), $Zr(OH)_4$ (Sigma–Aldrich, 97%), $Fe_2O_3$ (Sigma–Aldrich, 99.9%), $Mn_2O_3$ (Alfa Aesar, 99%), $SnO_2$ (Alfa Aesar, 99.9%), and CuO (Sigma–Aldrich, 99.99%) were used as precursors. All the precursors were stoichiometrically mixed in ethanol in 50 ml stainless steel jars at 200 rpm for 12 h in Retsch PM200 planetary ball mill. The mixture is then dried overnight and pelletized. These precursor pellets are then sintered at 1050 °C for 3 h in the air in the alumina tube furnace. (10% more $Li_2CO_3$ was added to compensate for possible loss during synthesis). Similar processes were performed to synthesize all HE-DRX oxides in an inert atmosphere.

### 2.4. Powder X-ray Diffraction

X-ray powder diffraction of all the synthesized samples was performed using a laboratory Bruker D8 Advance diffractometer operating at 40 kV and 40 mA with Cu K$\alpha$ radiation ($\lambda$ = 1.5418 Å). XRD profiling was collected by scanning from 10° to 80°, 2$\theta$, using a step size of 0.019°, at a rate of $2.6 \times 10^{-5}$ °/min 2$\theta$, in a custom air-free sample holder to avoid contamination from the air. Pawley refinement of the XRD patterns was performed using JANA2006. Particle morphology was observed by Scanning electron microscopy (JEOL JSM-6610LV) equipped with EDS (Oxford Instruments) operating at 20 kV.

## 3. Results

### 3.1. High Throughput Screening on Selected Prototype Formulas

Based on commonly reported stoichiometries of DRX positive electrode materials,[9,10,14] we sampled typical Li contents and F concentrations, resulting in the development of six prototype formulas (as shown in **Figure 1a**). At fixed Li and F concentrations, six metal species are placed at the M site in similar mole ratios to maximize configuration entropy and satisfy integer atoms per species as constrained by the supercell.[6] The stoichiometry of the metals is provided in Table S1 (Supporting Information). To search for HE-DRX materials, by considering the cost and atomic size, noble metals along with Sc, Hf, Ta, Ga, In, Y, as well as Co and Ni, were excluded. Apart from Li, 6 non-redox metals (Mg, Ti, Zr, Nb, Sn, and Sb) and 7 redox metals (V, Cr, Mn, Cu, Mo, W, Fe) are picked to enumerate the metal site. All typical oxidation numbers of the 7 redox metals are included during the enumeration.

Two types of structures are generated to account for the effect of the disorder. The first type of structure is generated based on the definition of Special quasi-random structures (SQS), which serve as an approximation of a fully random structure.[23] The inclusion of SQS structures reflects the recent discovery that HE-DRX structures are, in general, closer to fully random states compared with low entropy DRX.[7,24,25] In addition to SQS structures, we also included those representing electrostatic ground states (ESGS), which are considered as the approximation for structures exhibiting chemical short-range order.[11] As many DRX are identified to present significant short-range order,[9] the including of ESGS state will be useful to consider those HE-DRX that have predominant short-range order states. The lower energy of ESGS and SQS state is used to assess the stability of specific HE-DRX composition. As a result, we generated 6516 entries for $Li_{48}M_{32}O_{80}$, 276 entries for $Li_{48}M_{32}O_{64}F_{16}$, 9880 entries for $Li_{21}M_{15}O_{36}$, 776 entries for $Li_{21}M_{15}O_{30}F_6$, 1338 entries for $Li_{24}M_{12}O_{30}F_6$, and 24 entries for $Li_{24}M_{12}O_{24}F_{12}$. The specific metal elements for each formula are detailed in Figure 1b-g.

### 3.2. Redox Compatibility

Although the generation of combinatorial compositional space and structural enumeration assumes specific oxidation numbers for different cations, it is not guaranteed that these elements

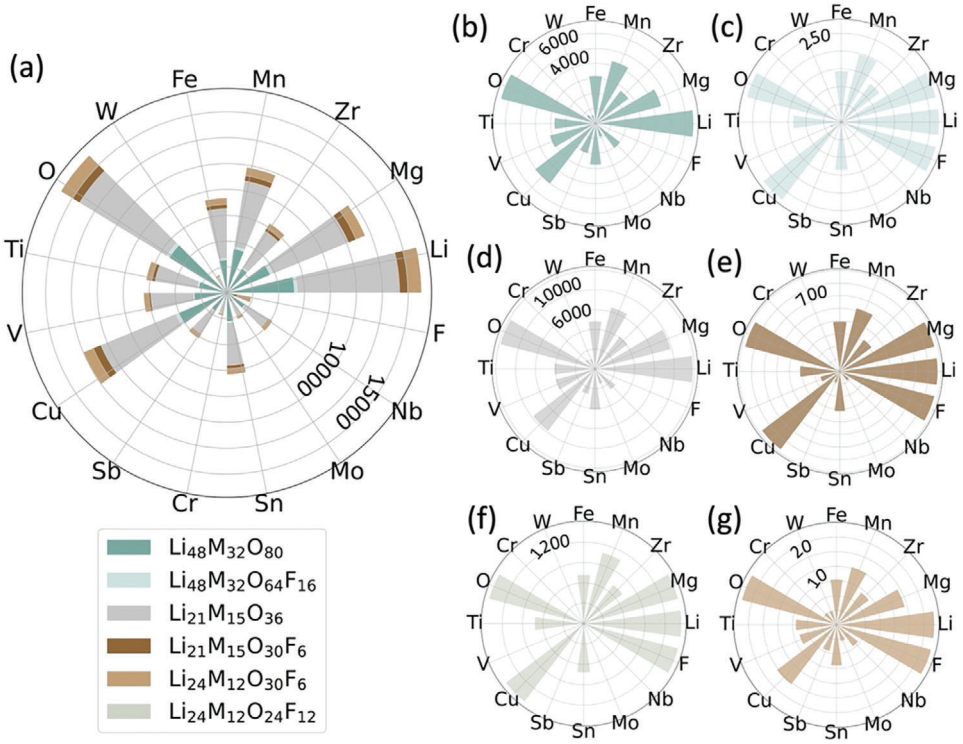


**Figure 1.** a) The barplot showing the number of compounds containing specific metal in the presented HE-DRX dataset; b-g) The barplot showing the number of compounds containing the specific metal in each chemical formula, b)$Li_{48}M_{32}O_{80}$; c) $Li_{48}M_{32}O_{64}F_{16}$; d) $Li_{21}M_{15}O_{36}$; e) $Li_{21}M_{15}O_{30}F_6$; f) $Li_{24}M_{12}O_{30}F_6$; g) $Li_{24}M_{12}O_{24}F_{12}$.

will maintain the same oxidation number after DFT relaxation. Therefore, a critical step following the acquisition of DFT results is determining the oxidation numbers of various ions. Maintaining charge neutrality in the bulk material is commonly employed as a constraint to assist in identifying the charge states. This constraint can then be used alongside molecular orbital theory to determine the actual charge states of all ions after DFT energy optimization. According to crystal orbital theory, the d states in transition metals split into three $t_{2g}$ orbitals and two $e_g$ orbitals for octahedron coordination as in HE-DRX (**Figure 2**a; Figure S2, Supporting Information). The extra d electrons on $M^{a+}$ gradually fill these five orbitals. The specific way these orbitals are filled then determines the actual magnetic moment of the cation. Conversely, by using the DFT-optimized magnetic moment, the actual oxidation state can be determined.

However, two types of ambiguity complicate the direct assignment of oxidation states from magnetic moments. The first arises from the fact that the same magnetic moment of an element can correspond to different oxidation states. The electron configurations of different oxidation states for V, Cr, Mo, W, and Mn are shown in Figure S2 (Supporting Information). The identification of oxidation states for these elements is straightforward as each specific magnetic moment corresponds uniquely to a single oxidation state. However, as demonstrated in Figure 2a, determining the specific oxidation states for Cu and Fe is quite challenging. For example, a magnetic moment of 4 $\mu_B$ for Fe could correspond to either $Fe^{2+}$ and $Fe^{4+}$, while a magnetic moment of 0 $\mu_B$ for Cu could correspond to either $Cu^{+}$ and $Cu^{3+}$. Furthermore, due to the disordered coordination environments and the diverse covalency of M-O bonds in HE-DRX, the DFT-calculated magnetic moments appear as a distribution rather than a fixed value. For redox centers like Mn, Cu, and Fe, the distribution of magnetic moments for different oxidation states can overlap (Figure S4, Supporting Information). To address these challenges, a robust algorithm that adheres to molecular orbital rules and aims to maximize the number of charge-balanced structures has been developed and is presented in Figure 2b and Note S1(Supporting Information). With the application of this algorithm, 15204 out of 18810 structures are charge-balanced with the distribution of $E_{hull}$ values shown in Figure S3 (Supporting Information). The exact decision boundaries for different species can be found in Figure S4 (Supporting Information). Among the 18810 entries analyzed, 3606 failed to achieve charge balance, we hypothesize that this discrepancy may arise from delocalization of electrons, which may deserve further study separately.

### 3.3. Stability of Redox Centers

The establishment of a charge balance algorithm enables the study of stability among various redox centers. There are two types of stability perspectives related to redox centers: redox compatibility and phase stability. Redox compatibility indicates whether we can achieve our aimed oxidation state by cooperating with specific metals while phase stability determines whether specific elements can co-exist in the targeted single phase.

The redox compatibility is assessed by calculating the likelihood that two electron configurations of metal ions can co-

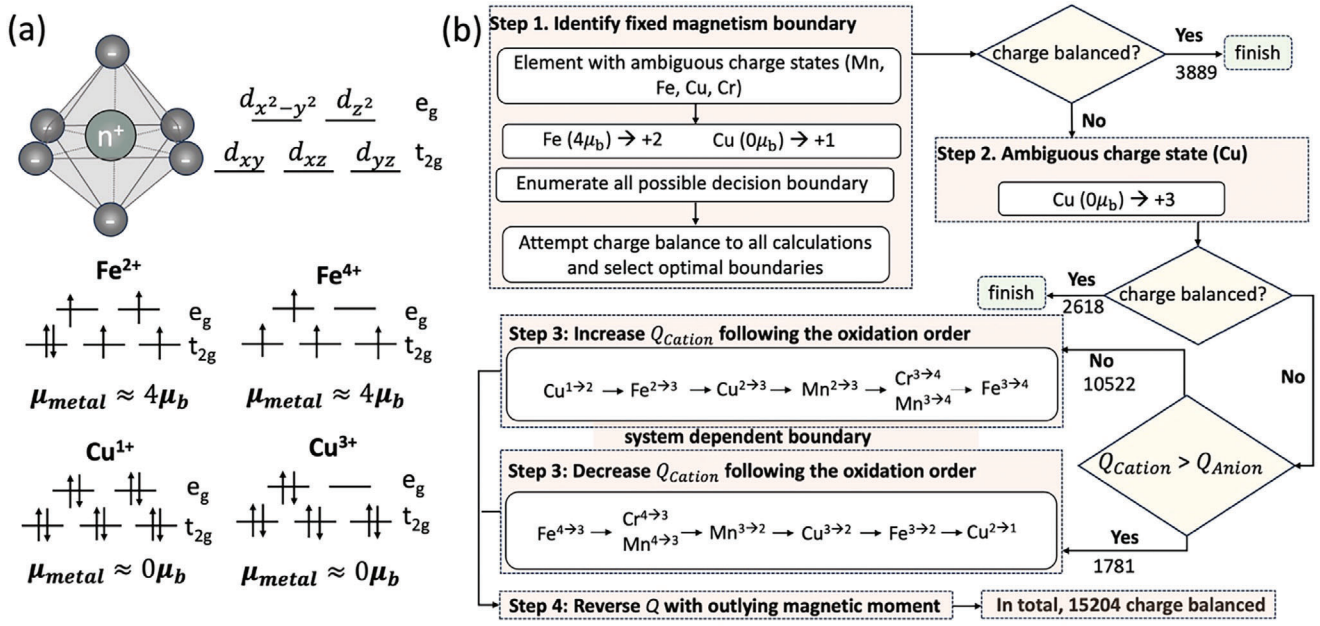


**Figure 2.** a) Molecular orbitals of cation coordination in DRX and two examples of ambiguous charge states for the same magnetic moment; b) The workflow that describes our charge state identification algorithm.

exist within a single phase based on our DFT dataset. The statistics of redox compatibility are compiled and presented in **Figure 3**. Two kinds of probabilities are computed to analyze trends in redox compatibility depending on the normalization of the observed number of compounds where $A^{m+}$ and $B^{n+}$ coexist. As indicated in Figure 3a, this normalization considers all compounds containing both elements A and B, represented as $P(A^{m+}B^{n+}|AB)$. When $A^{m+}$ and $B^{n+}$ refer to different oxidation states of the same element, it is represented as $P(A^{m+}A^{n+}|A)$. Conversely, Figure 3b shows the normalization based on all observations of $A^{m+}$, denoted as $P(A^{m+}B^{n+}|A^{m+})$.

Within the same elemental couple AB, the likelihood of forming $A^{m+}B^{n+}$ is shown in Figure 3a. In Figure 3a, the ions are ordered by atomic number and oxidation state. To illustrate some interesting comparisons, in the elemental couple Cr-Mn, $Cr^{3+}$-$Mn^{4+}$ and $Cr^{4+}$-$Mn^{4+}$ are more likely to form. At the same time, Cr species tend to stabilize more with $Mn^{4+}$ rather than $Mn^{3+}$ and will never get stabilized with $Mn^{2+}$. The stability between $Cr^{3+}$ and $Mn^{4+}$ can be supported by several low entropy DRX compositions that have been reported[26,27] recently; the fact that $Cr^{3+}$ can also be stabilized with $Mn^{3+}$ reveals that more redox flexibility and potentially higher metal redox capacity can be enabled by designing high entropy

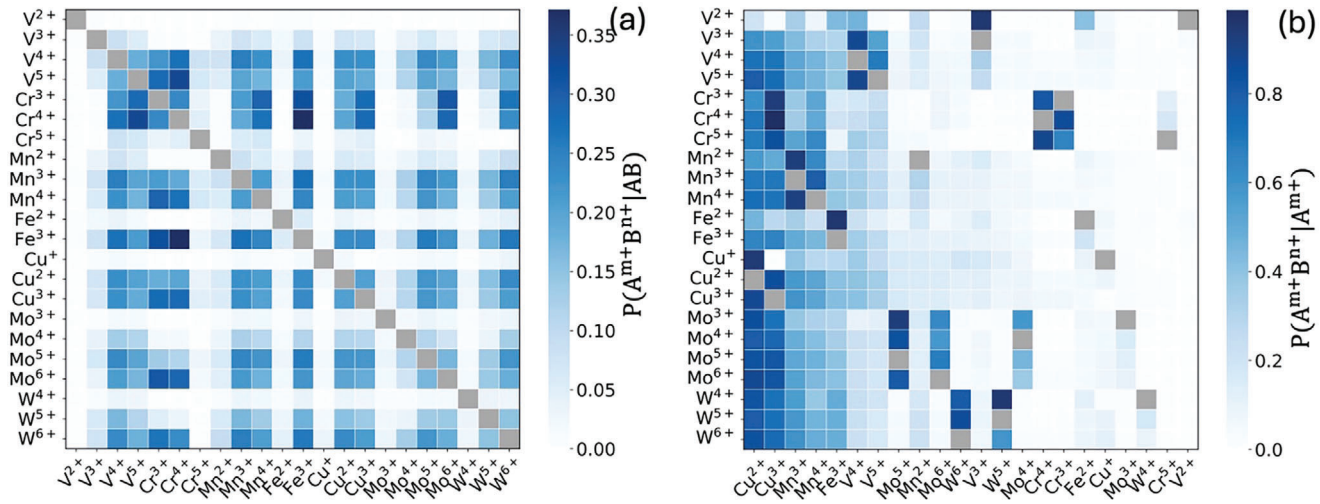


**Figure 3.** a) The heatmap illustrates the likelihood of each species pair occurring when the corresponding pair of elements is present; b) The heatmap shows the stability of other different species when there is a specific specie present.

composition. Moreover, due to the diverse local environments inherent in high-entropy materials, mixvalency is indeed a common feature in these systems. Mixvalency is observed in high entropy disordered rocksalt materials shown in Figure 3a when the species on x-axis and y-axis share the same element. For example, we observe $V^{3+}$ coexisting with $V^{4+}$, $Cr^{3+}$ coexisting with $Cr^{4+}$, $Mn^{3+}$ coexisting with $Mn^{4+}$, etc. The presence of multiple oxidation states for a single cation species contributes to the overall configurational entropy of the material, which can enhance its stability.

The relative stability between certain cation specie and all other species can then be visualized by dividing the occurrence of the specific occurrence of $A^{m+}B^{n+}$ by the total occurrence of $A^{m+}$. Additionally, the relative redox compatibility of different cation species in each column ($B^{n+}$) with the same element A but different oxidation numbers $A^{m+}$ can also be shown. As shown by Figure 3b, one overlooked redox specie, $Cu^{2+}$, shows reasonable stability across many typical redox centers, such as $Fe^{3+}$, $V^{4+}$, $Mn^{3+}$, $Cr^{4+}$, $Cr^{3+}$ and $Mo^{5+}$. In contrast, $Cu^{+}$ can only be stabilized in rare cases with limited redox centers ($Mo^{5+/6+}$, $W^{5+/6+}$). Particularly, both $Cu^{2+}$ and $Cu^{3+}$ show reasonable stability with $Mn^{3+}$, which is much better than the case of $Cu^{+}$-$Mn^{3+}$ pair. Some elements with two different oxidation states show reasonable compatibility: $Cu^{2+}/Cu^{3+}$, $Mn^{3+}/Mn^{4+}$, and $V^{4+}/V^{5+}$. This reveals that it is possible to couple $Cu^{2+} \rightarrow Cu^{3+}$, $Mn^{3+} \rightarrow Mn^{4+}$, $V^{4+} \rightarrow V^{5+}$ redox with other typical metal redox in positive electrode design. To achieve a more comprehensive understanding of chemical formula dependent stability across various ion species within high-entropy disordered rocksalt structures, compatibility maps were generated covering all prototype chemical formulas, as shown in Figures S5–S10 (Supporting Information). In general, Cr species exhibit a stronger tendency to stabilize with $Mn^{4+}$ rather than $Mn^{3+}$, which can be observed across most chemical formulas. Additionally, $Cu^{2+}$ and $Cu^{3+}$ are found to be compatible with typical redox centers across all formulas.

In addition to redox compatibility, the phase stability of compounds with specific redox center $M^{n+}$ is evaluated using energy above hull ($E_{hull}$).[7,28,29] To quantify the likelihood of having a certain redox center, the probability of finding $M^{n+}$ with $E_{hull} < 0$ at a certain temperature T is defined as $P_{E_{hull,T}}(M^{n+})$. This is calculated as the ratio of the number of compounds where $n_{E_{hull,T}(M^{n+}) \leq 0}$ to the total occurrences of $M^{n+}$, $n(M^{n+})$. The $E_{hull}$ is determined using DFT to compute the total energy relative to all ordered competing phases from phase diagram calculations.[7,28,29] The effect of temperature is accounted for by incorporating ideal mixing entropy, following approaches used in previous literature.[7,28,29] The count of compounds meeting the $E_{hull}$ criterion, $n_{E_{hull,T}(M^{n+}) \leq 0}$, and the occurrence of $M^{n+}$ in a dataset of 15204 charge-balanced compounds are used to compute $P_{E_{hull,T}}(M^{n+})$. This probability was evaluated across different prototype formulas and is shown in **Figure 4**.

As indicated in Figure 4, only the species that appear in the compounds with $E_{hull} < 0$ at a certain temperature T are shown in the circular barplot. In most cases, the temperature is set to 1473K, which is the typical upper bound of solid-state synthesis temperature. However, for HE-DRX with high F contents, e.g. $Li_{48}M_{32}O_{64}F_{16}$ and $Li_{24}M_{12}O_{24}F_{12}$, no compounds exhibit negative energy above the hull ($E_{hull}$) at 1473 K. Therefore, the temperature is increased to 1673 K to access the stability order.

Several stoichiometry dependencies of elemental stability can be observed from Figure 4. Particularly, $Fe^{2+}/Fe^{3+}$ appears to be an overlooked species that can be stabilized in HE-DRX. $Fe^{3+}$ tends to be a stable element across all chemical formula prototypes. In contrast, $Fe^{2+}$ is only observed as a top element for oxides, while in all four types of oxy-fluoride stoichiometry, $Fe^{2+}$ is computed to be a much less stable element. Moreover, it appears that the stability of $Cr^{3+}$ is quite dependent on the specific stoichiometry. Specifically, it is generally more stable in both oxide prototypes, e.g., $Li_{21}M_{15}O_{36}$ and $Li_{48}M_{32}O_{80}$, but become much less stable in oxyfluorides. However, where enough Li-excess level is presented, such as in the case of $Li_{24}M_{12}O_{30}F_6$, both $Cr^{3+}$ and $Cr^{4+}$ show up as a stable specie again. In addition to the stoichiometry dependency of elemental stability, it is also identified that W, V, and Mo species, being species that are redox active, show less stability than Mn, Fe, Cr and Cu. This instability is more significant when W, V, and Mo ions are coupled; all the compounds exhibit instability (showing a positive $E_{hull}$) at 1473K (Figure S11, Supporting Information).

### 3.4. Stability of Charge Compensators

In addition to examining the stability of redox centers, it is also worth investigating the stability of various charge compensators. The distribution of $E_{hull,1473K}$ for five redox-inactive charge compensators is demonstrated in **Figure 5a**. Surprisingly, many stable compounds utilize $Sb^{5+}$ as a charge compensator. The preference for $Sb^{5+}$ is even more pronounced than for $Nb^{5+}$ and $Ti^{4+}$, which are widely used in state-of-the-art DRX positive electrodes.[7,9,10,14,30,31] This unprecedented discovery highlights the overlooked potential of $Sb^{5+}$ as a charge compensator. Furthermore, it should be noted that Sb is also cheaper compared to Nb,[32] suggesting that the cost of materials in DRX positive electrodes can be further reduced by incorporating $Sb^{5+}$. The stability of charge compensators across different redox centers is shown in Figure S12 (Supporting Information). $Mn^{2+}$, $Cr^{3+}$, $Fe^{2+}$ show the best stability with five charge compensators. Other species, including $Fe^{3+}$, $Mn^{3+}$, $Mn^{4+}$, $Cr^{4+}$, $V^{2+}$, $Cu^{+}$, and $Cu^{2+}$, exhibit reasonable stability across various redox centers. In addition to the general stability trend, the top three competing phases for all five charge compensators and the corresponding observed frequencies are also shown in Figure 5b,c. It can be inferred that for all five species, the most frequently seen competing phases are ordered versions of the rocksalt structure, e.g. $Li_3SbO_4$, $Li_3NbO_4$, $Li_2TiO_3$, $Li_2ZrO_3$, and $Li_2SnO_3$. Therefore, the relative stability of such charge compensators is largely dictated by the tendency of forming ordered rocksalt structures.

## 4. Discussion

### 4.1. Overlooked Chemical Space for DRX

Among the 9405 compositions in our DRX positive electrode materials dataset, 1215 compositions exhibit stabilization

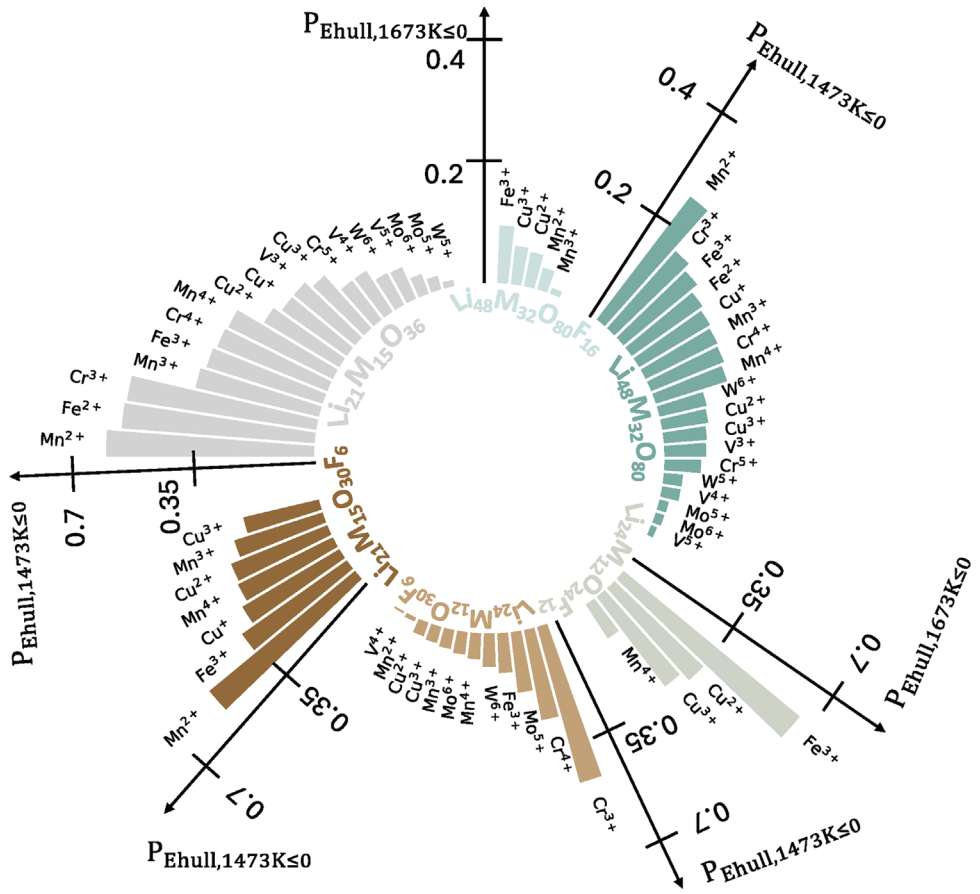


**Figure 4.** The circular bar plot represents the stability trend of redox centers in each chemical formula.

temperatures lower than 1326.2 K, which is the calculated stabilization temperature of widely reported low entropy DRX material $Li_{1.2}Mn_{0.4}Ti_{0.4}O_2$,[33,34] as shown in Figure S1 (Supporting Information). These results indicate the competitive thermodynamic stability compared to the $Li_{1.2}Mn_{0.4}Ti_{0.4}O_2$ material. Moreover, high-entropy materials inherently offer advantages such as improved Li percolation, enhanced Li-ion kinetics, reduced critical elements (Co/Ni), and reduced volume changes during cycling,[6,12,13] making them more promising positive electrode materials.

We have summarized the reported Li-ion rocksalt materials[7,35–40] with the overlooked redox specie Cu, along with five charge compensators considered in this work as **Figure 6a**. The reported Li-ion rocksalt positive electrode compounds are listed in Table S2 (Supporting Information). Moreover, the chord diagram in Figure 6b illustrates the frequency with which

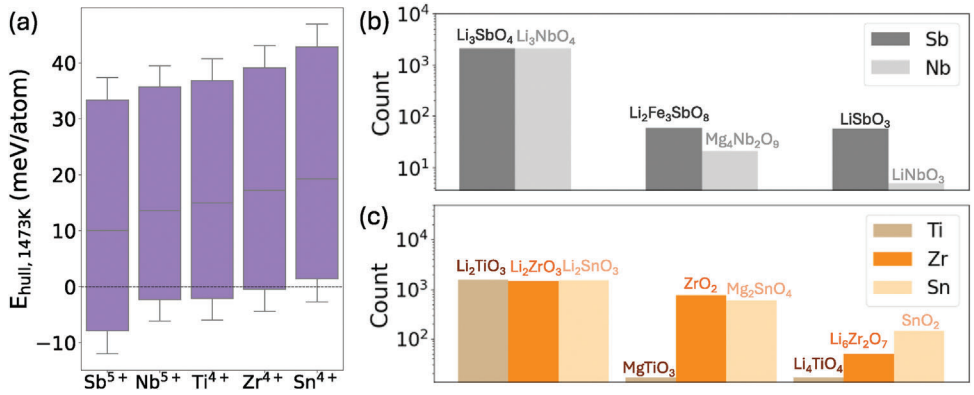


**Figure 5.** a) Distribution of the $E_{hull}$ at 1473K for different redox-inactive charge compensators; b) The top 3 competing phases for Sb and Nb contained HE-DRX; c) The top 3 competing phases for Ti/Zr/Sn contained HE-DRX.

 

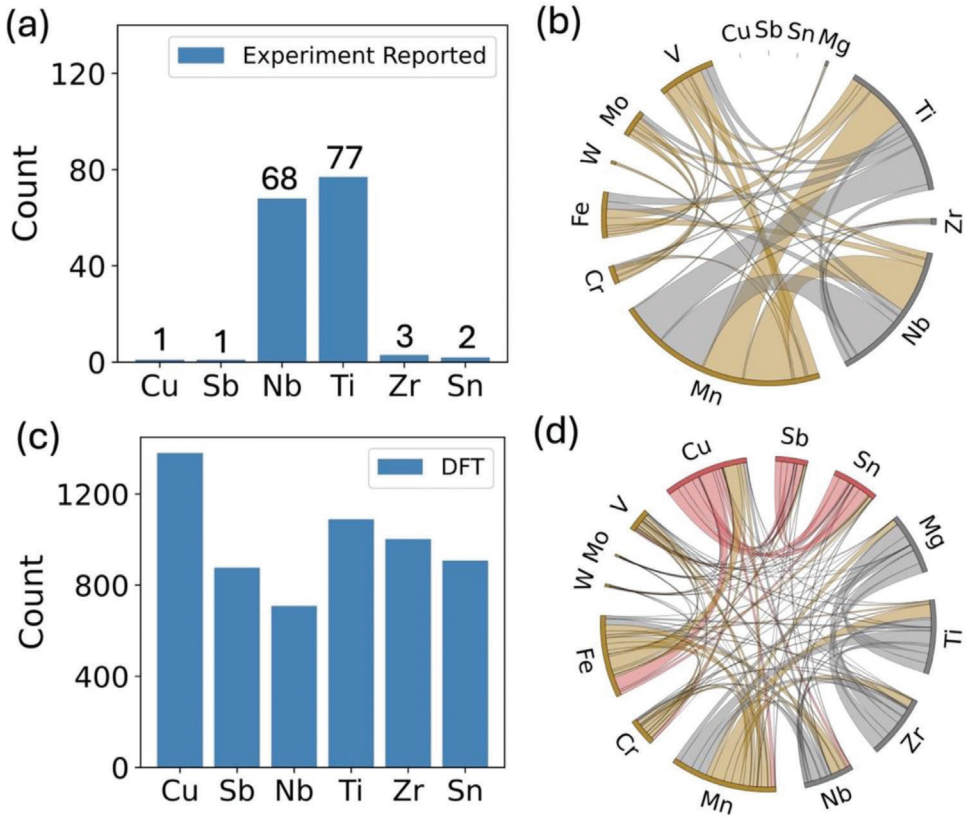


**Figure 6.** a) The number of HE-DRX reported in previous experimental research which contains Cu, Sb, Nb, Ti Zr and Sn; b) The chord diagram of elemental compatibility based on experimentally reported compositions; c) The number of HE-DRX in our calculations which contains Cu, Sb, Nb, Ti Zr and Sn and with $E_{hull,1473K} < 0$; d) The chord diagram of elemental compatibility based on our DFT calculations with $E_{hull,1473K} < 0$; For both chord diagrams in (b) and (d), the width of the connections between two elements is proportional to the probability of these two elements to co-exist in a compound reported in experiment or a compound with $E_{hull,1473K} < 0$. The overlooked elements are highlighted in red, other redox centers are shown in yellow, and the remaining charge compensators are marked in grey. Each elemental pair is represented by two connections, with each color corresponding to one of the two elements.

different metal pairs are reported across all elements considered in this work. The width of each connection is proportional to the frequencies with which two elements coexist in a single phase, as reported in experimental literature. It is evident that most of the materials reported in the literature contain Mn, Ti and Nb, followed by V, Fe and Cr.

For comparison, we plotted the number of synthetically accessible compounds from our DFT dataset (with $E_{hull,1473K} \leq 0$) that contain the overlooked redox specie Cu, along with five charge compensators in Figure 6c. In our dataset, the number of entries containing Sb and Nb is 2584 each, while the number of entries containing Ti, Zr and Sn is 3946 each. Although Sb and Nb show fewer stable compositions, the overall stability trend aligns with that shown in Figure 5a. Furthermore, the chord diagram of elemental stability generated from our DFT dataset is visualized in Figure 6d, where the width of the connections represents the probability of finding a compound with $E_{hull,1473K} \leq 0$ containing both elements. Interestingly, the pair preferences in Figure 6d differ significantly from the experimental coverage shown in Figure 6b. Figure 6d reveals that Cu-based DRX has comparable synthetical accessibility compared to Mn-based DRX. Moreover, while V- and Cr- based compounds are frequently investigated in the literature, as shown in Figure 6d, they are not particularly stable. Consistent with studies by Kitchaev et.al.,[37] and Huang et. al.,[26,30] as well as systematic data mining shown in Figure 6d, both V- and Cr-based DRX require high-energy ball milling to form DRX phases, as conventional solid-state reactions up to 1473 K is insufficient to form DRX structures. Additionally, in contrast to the extensive investigation of Nb- and Ti-based DRX in the literature, Sb- and Sn-based DRX exhibit reasonable stability comparable to Nb-based DRX. This highlights the overlooked potential of utilizing Sb and Sn in the design of DRX positive electrodes.

In terms of the physical or chemical origins of stability for such compounds, the Shannon radii in an octahedral environment[41] for $Cu^{+}$ (0.77 Å), $Cu^{2+}$ (0.73 Å), and $Cu^{3+}$ (0.54 Å) are quite close to typical redox centers, such as $Mn^{2+}$ (0.83 Å) and $Mn^{3+}$ (0.645 Å). This similarity suggests that Cu in various oxidation states can be compatible in terms of ionic size with other common species. Similarly, $Sb^{5+}$ (0.6 Å) and $Sn^{4+}$ (0.69 Å) have radii comparable to those of $Nb^{5+}$ (0.64 Å) and $Ti^{4+}$ (0.605 Å), which are commonly utilized reported DRX positive electrodes. These ionic radii similarity highlights the potential reason of broad stability of Cu, Sb, and Sn in our screened HE-DRX space. Also, the stability of Cu,

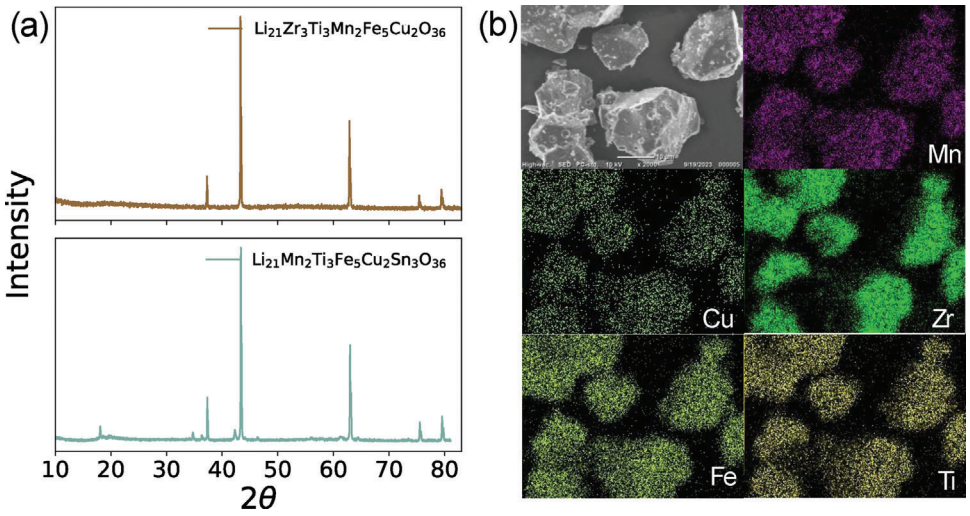


**Figure 7.** a) The XRD diffraction pattern of $Li_{21}Zr_3Ti_3Mn_2Fe_5Cu_2O_{36}$ and $Li_{21}Mn_2Ti_3Fe_5Cu_2Sn_3O_{36}$. b) The SEM image and EDS elemental mapping figures of $Li_{21}Zr_3Ti_3Mn_2Fe_5Cu_2O_{36}$. The mapping results for Mn, Cu, Zr, Fe, and Ti are presented in different colors.

Sb and Sn in various HE-DRX compositions offers richer tunable chemical space to avoid or minimize the cobalt and nickel content in HE-DRX. Particularly, Cu redox can also be a viable replacement for Co and Ni redox in classic Li-ion positive electrodes.

### 4.2. Experimental Verification of Stability Prediction

To verify the reliability of the computational metrics and elemental rules established, two new HE-DRX compositions predicted from our dataset were synthesized by solid-state reactions: $Li_{21}Zr_3Ti_3Mn_2Fe_5Cu_2O_{36}$ and $Li_{21}Mn_2Ti_3Fe_5Cu_2Sn_3O_{36}$. These compounds are chosen with computed $E_{hull,1473K}$ to be −4.948 meV/atom and −0.632 meV/atom, respectively. Selection was initiated by randomly picking compounds with Cu and Fe that are predicted to be stable at 1473 K, as both redox centers are infrequently studied in previous literature. Additionally, these include less favorable charge compensators, $Zr^{4+}$ and $Sn^{4+}$, chosen because compounds with these compensators are expected to be stable only in limited compositions, as indicated in Figures 5 and 6. Therefore, the successful synthesis of these compound can be a strong support to the reliability of our computational approach. Pawley refinements are applied on two XRD diffraction patterns, as shown in Figure S13 (Supporting Information). The successful synthesis of compounds in more challenging chemical space helps validate the reliability of our computational metric.

As shown in **Figures** 7a and S13 (Supporting Information), both compounds were synthesized with neglectable impurities. Complementing the x-ray diffraction (XRD) results, scanning electron microscopy-based energy-dispersive spectroscopy (SEM-EDS) images are presented in Figure 7b. The EDS results indicate a homogenous distribution of all elements across the particles ranging from 10 to 20 μm. This supports the conclusion that the predicted materials were synthesized with a homogenous elemental distribution.

## 5. Conclusion

We have developed a comprehensive dataset of Li-ion high entropy rocksalt-type positive electrode materials, spanning a space of 28 metal species. This dataset includes six reported formulas with various concentrations of Li and F, and two types of ionic orderings. In total, our dataset comprises 18810 entries of materials. Through systematic data mining of elemental stability, we have highlighted the overlooked potential of utilizing Cu, Sn and Sb in HE-DRX design, showing comparable stability to Mn-, Nb-, Ti-based DRX, with the added potential to reduce elemental cost. Supported by experimental verification, our work offers valuable insights into the rational stability prospects for designing HE-DRX-based Li-ion positive electrode.

## Supporting Information

Supporting Information is available from the Wiley Online Library or from the author.

## Acknowledgements

L.W. and N.S. contributed equally to this work. L.W. and B.O. would like to acknowledge funding support from Samsung Global Research Opportunity. The Computational resources are provided by the Advanced Cyberinfrastructure Coordination Ecosystem: Services & Support (ACCESS), the National Energy Research Scientific Computing Center (NERSC), a DOE Office of Science User Facility supported by the Office of Science and the U.S. Department of Energy under contract no. DE-AC02-05CH11231 and Research Computing Center (RCC) at Florida State University. The computation and data processing are also supported by the supercomputing resources from the Department of Energy's Office of Energy Efficiency and Renewable Energy at the National Renewable Energy Laboratory.

## Conflict of Interest

The authors declare no conflict of interest.

## Data Availability Statement

The data that support the findings of this study are available from Samsung SDI. Restrictions apply to the availability of these data, which were used under license for this study. Data are available from the authors with the permission of Samsung SDI.

## Keywords

cobalt and nickel-free positive electrode, data-driven stability rules, high entropy disordered rocksalt, overlooked stable species

Received: October 25, 2024
Revised: January 22, 2025
Published online:

[1] N. Nitta, F. Wu, J. T. Lee, G. Yushin, *Mater. Today* **2015**, *18*, 252.
[2] R. Schmuch, R. Wagner, G. Hörpel, T. Placke, M. Winter, *Nat. Energy* **2018**, *3*, 267.
[3] T. Placke, A. Heckmann, R. Schmuch, P. Meister, K. Beltrop, M. Winter, *Joule* **2018**, *2*, 2528.
[4] M. Li, J. Lu, Z. Chen, K. Amine, *Adv. Mater.* **2018**, *30*, 1800561.
[5] A. Manthiram, *J. Phys. Chem. Lett.* **2011**, *2*, 176.
[6] B. Ouyang, Y. Zeng, *Nat. Commun.* **2024**, *15*, 973.
[7] Z. Lun, B. Ouyang, D. H. Kwon, Y. Ha, E. E. Foley, T. Y. Huang, Z. Cai, H. Kim, M. Balasubramanian, Y. Sun, J. Huang, Y. Tian, H. Kim, B. D. McCloskey, W. Yang, R. J. Clement, H. Ji, G. Ceder, *Nat. Mater.* **2021**, *20*, 214.
[8] Y. Zeng, B. Ouyang, J. Liu, Y. W. Byeon, Z. Cai, L. J. Miara, Y. Wang, G. Ceder, *ScienceScience* **2022**, *378*, 1320.
[9] B. Ouyang, N. Artrith, Z. Lun, Z. Jadidi, D. A. Kitchaev, H. Ji, A. Urban, G. Ceder, *Adv. Energy Mater.* **2020**, *10*, 1903240.
[10] Z. Lun, B. Ouyang, Z. Cai, R. J. Clément, D.-H. Kwon, J. Huang, J. K. Papp, M. Balasubramanian, Y. Tian, B. D. McCloskey, H. Ji, H. Kim, D. A. Kitchaev, G. Ceder, *Chem-Us* **2020**, *6*, 153.
[11] L. Li, B. Ouyang, Z. Lun, H. Huo, D. Chen, Y. Yue, C. Ophus, W. Tong, G. Chen, G. Ceder, C. Wang, *Nat. Commun.* **2023**, *14*, 7448.
[12] Y. Zeng, B. Ouyang, J. Liu, Y.-W. Byeon, Z. Cai, L. J. Miara, Y. Wang, G. Ceder, *ScienceScience* **2022**, *378*, 1320.
[13] X. Zhao, Y. Tian, Z. Lun, Z. Cai, T. Chen, B. Ouyang, G. Ceder, *Joule* **2022**, *6*, 1654.
[14] R. J. Clément, Z. Lun, G. Ceder, *Energy Environ. Sci.* **2020**, *13*, 345.
[15] G. Kresse, D. Joubert, *Phys. Rev. B* **1999**, *59*, 1758.
[16] G. Kresse, J. Furthmüller, *Comput. Mater. Sci.* **1996**, *6*, 15.
[17] S. L. Dudarev, G. A. Botton, S. Y. Savrasov, C. J. Humphreys, A. P. Sutton, *Phys. Rev. B* **1998**, *57*, 1505.
[18] L. Wang, T. Maxisch, G. Ceder, *Phys. Rev. B* **2006**, *73*, 195107.
[19] A. Jain, S. P. Ong, G. Hautier, W. Chen, W. D. Richards, S. Dacek, S. Cholia, D. Gunter, D. Skinner, G. Ceder, K. A. Persson, *APL Mater.* **2013**, *1*, 011002.
[20] W. Sun, S. T. Dacek, S. P. Ong, G. Hautier, A. Jain, W. D. Richards, A. C. Gamst, K. A. Persson, G. Ceder, *Sci. Adv.* **2016**, *2*, e1600225.
[21] B. Ouyang, J. Wang, T. He, C. J. Bartel, H. Huo, Y. Wang, V. Lacivita, H. Kim, G. Ceder, *Nat. Commun.* **2021**, *12*, 5752.
[22] L. Wang, J. Wang, B. Ouyang, *Adv. Energy Mater.* **2023**, *13*, 2302584.
[23] A. Zunger, S. Wei, L. G. Ferreira, J. E. Bernard, *Phys. Rev. Lett.* **1990**, *65*, 353.
[24] L. Wang, Z. He, B. Ouyang, *Comp. Mater. Sci.* **2023**, *230*, 112513.
[25] L. Wang, T. He, B. Ouyang, *ChemRxiv* **2024**, https://doi.org/10.26434/chemrxiv-2024-fmq8p.
[26] J. Huang, P. Zhong, Y. Ha, D.-H. Kwon, M. J. Crafton, Y. Tian, M. Balasubramanian, B. D. McCloskey, W. Yang, G. Ceder, *Nat. Energy* **2021**, *6*, 706.
[27] Z. Cai, B. Ouyang, H.-M. Hau, T. Chen, R. Giovine, K. P. Koirala, L. Li, H. Ji, Y. Ha, Y. Sun, J. Huang, Y. Chen, V. Wu, W. Yang, C. Wang, R. J. Clément, Z. Lun, G. Ceder, *Nat. Energy* **2023**, *9*, 27.
[28] B. Ouyang, J. Wang, T. He, C. J. Bartel, H. Huo, Y. Wang, V. Lacivita, H. Kim, G. Ceder, *Nat. Commun.* **2021**, *12*, 5752.
[29] Y. Chen, Z. Lun, X. Zhao, K. P. Koirala, L. Li, Y. Sun, C. A. O'Keefe, X. Yang, Z. Cai, C. Wang, H. Ji, C. P. Grey, B. Ouyang, G. Ceder, *Nat. Mater.* **2024**, *23*, 535.
[30] J. Huang, B. Ouyang, Y. Zhang, L. Yin, D. H. Kwon, Z. Cai, Z. Lun, G. Zeng, M. Balasubramanian, G. Ceder, *Nat. Mater.* **2023**, *22*, 353.
[31] Z. Lun, B. Ouyang, D. A. Kitchaev, R. J. Clément, J. K. Papp, M. Balasubramanian, Y. Tian, T. Lei, T. Shi, B. D. McCloskey, J. Lee, G. Ceder, *Adv. Energy Mater.* **2018**, *9*, 1802959.
[32] B. J. Watson, R. G. Eggert, *Journal of Industrial Ecology* **2020**, *25*, 890.
[33] L. Li, B. Ouyang, Z. Lun, H. Huo, D. Chen, Y. Yue, C. Ophus, W. Tong, G. Chen, G. Ceder, C. Wang, *Nat. Commun.* **2023**, *14*, 7448.
[34] H. Ji, A. Urban, D. A. Kitchaev, D.-H. Kwon, N. Artrith, C. Ophus, W. Huang, Z. Cai, T. Shi, J. C. Kim, H. Kim, G. Ceder, *Nat. Commun.* **2019**, *10*, 592.
[35] H. Li, R. Fong, M. Woo, H. Ahmed, D.-H. Seo, R. Malik, J. Lee, *Joule* **2022**, *6*, 53.
[36] N. Twu, X. Li, A. Urban, M. Balasubramanian, J. Lee, L. Liu, G. Ceder, *Nano Lett.* **2015**, *15*, 596.
[37] Q. Wang, A. Sarkar, D. Wang, L. Velasco, R. Azmi, S. S. Bhattacharya, T. Bergfeldt, A. Düvel, P. Heitjans, T. Brezesinski, H. Hahn, B. Breitung, *Energy Environ. Sci.* **2019**, *12*, 2433.
[38] M. Sathiya, A. M. Abakumov, D. Foix, G. Rousse, K. Ramesha, M. Saubanere, M. L. Doublet, H. Vezin, C. P. Laisa, A. S. Prakash, D. Gonbeau, G. VanTendeloo, J. M. Tarascon, *Nat. Mater.* **2015**, *14*, 230.
[39] R. Wang, X. Li, L. Liu, J. Lee, D.-H. Seo, S.-H. Bo, A. Urban, G. Ceder, *Electrochem. Commun.* **2015**, *60*, 70.
[40] J. Lee, D. A. Kitchaev, D. H. Kwon, C. W. Lee, J. K. Papp, Y. S. Liu, Z. Lun, R. J. Clement, T. Shi, B. D. McCloskey, J. Guo, M. Balasubramanian, G. Ceder, *NatureNature* **2018**, *556*, 185.
[41] R. D. Shannon, *Foundations of Crystallography* **1976**, *32*, 751.

 